Large amplitude wavefront generation and correction with membrane mirrors

Peter Kurczynski

Bell Labs, Lucent Technologies, Murray Hill NJ 07974
kraken@lucent.com

Harold M. Dyson

Bell Labs, Lucent Technologies, Murray Hill NJ 07974
hdyson@lucent.com

Bernard Sadoulet

University of California, Berkeley CA 94720
sadoulet@cosmology.berkeley.edu

Abstract: Membrane mirror devices presented here are capable of large amplitude deformation for wavefront generation and correction in adaptive optics. These devices consist of micro-fabricated membranes that are actuated by an underlying electrode array and a transparent counter-electrode. Deformations of +/- 20 μm optical are demonstrated for low order deformations and 10 μm optical for high order Zernike polynomial wavefront generation. Large deformation at low voltage is enabled by the use of low stress membranes, relatively small membrane-electrode separation and the transparent counter-electrode.

OCIS codes: (010.1080) Adaptive optics; (230.6120) Spatial light modulators ; (010.1330) (230.4000) Microstructure fabrication; Atmospheric turbulence; (170.4460) Ophthalmic optics

References and Links

1. Marc Séchaud, "Wave-front compensation devices," in F. Roddier, ed. *Adaptive Optics in Astronomy,* (Cambridge University Press, Cambridge, 1999).
2. G. Vdovin, and P. M. Sarro, "Flexible mirror micromachined in silicon," Applied Optics **34**, 2968-2972 (1995).
3. C. Paterson, I. Munro and J. C. Dainty, "A low cost adaptive optics system using a membrane mirror," Optics Express **6**, 175-185 (2000).
4. I. Iglesias and P. Artal, "Closed loop adaptive optics in the human eye," Optics Letters **26**, 746-748 (2001).
5. L. Zhu et al., "Wave-front generation of Zernike polynomial modes with a micromachined membrane deformable mirror" Applied Optics, **38**, 6019-6026 (1999).
6. L. Zhu et al., "Adaptive control of a micromachined continuous-membrane deformable mirror for aberration compensation," Applied Optics, **38**, 168-178 (1999).
7. D. Dayton et al., "Laboratory and field demonstration of a low cost membrane mirror adaptive optics system," Opt. Comm. **176**, 339-345 (2000).
8. R. P. Grosso and M. Yellin, "Membrane mirror as an adaptive optical element," J. Opt. Sci. Am. **67**, 399-406 (1977).
9. Pierre-Yves Madec, "Control techniques," in F. Roddier, ed. *Adaptive Optics in Astronomy,* (Cambridge University Press, Cambridge, 1999).
10. J.C.Wyant and K. Creath, "Basic Wavefront Aberration Theory for Optical Metrology" in *Applied Optics and Optical Engineering*, J. C. Wyant and R. R. Shannon, eds. (Academic, New York, NY 1992).
11. P. Kurczynski and B. Sadoulet are preparing a manuscript to be called "Stability of Electrostatic Actuated Membrane Mirror Devices."

1. Introduction

Deformable mirrors made from tensioned membranes have a long history of use as wavefront correctors for adaptive optics.[1] The membrane is mechanically supported at its periphery and suspended a fixed distance above an actuating electrode plane. Relatively inexpensive micro-fabricated membrane mirrors have been used in a variety of adaptive optics applications.[2] These devices have been successful as inexpensive correctors for comparatively mild optical distortions;[3] however, they have not demonstrated the large range of deformation required for complete wavefront correction in applications such as retinal imaging and vision correction,[4,5,6] and atmospheric turbulence compensation.[7] Segmented and continuous-face sheet micro-fabricated deformable mirrors have also been fabricated for a variety of applications; however, at present these devices are similarly limited in the stroke they can achieve.

Here we report membrane mirrors that are capable of significantly greater amplitude of deformation than previous devices. Large deformation is enabled by the low intrinsic stress of the membrane, small membrane-electrode gap spacing, and the use of a transparent electrode, as discussed below. These devices have generated +/- 20 μm peak-to-valley optical wavefront deformation for low order deformations, and nearly 10 μm peak-to-valley optical deformation for high order deformations. For high spatial order deformations, this figure is an order of magnitude improvement over previous micro-fabricated membrane mirrors.

A membrane mirror device is illustrated in Figure 1a. The membrane mirror is positioned between the transparent electrode and an underlying electrode array. This actuating electrode array contains 1024 electrodes that are each driven by off chip D/A electronics.
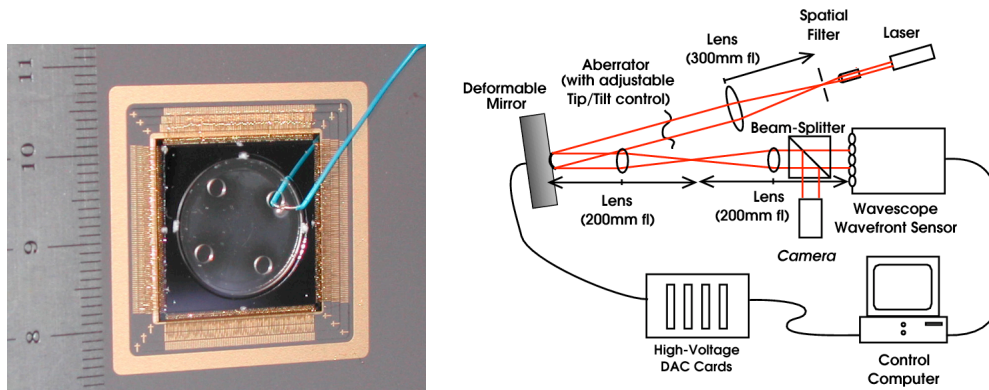

Figure 1a,b. Left figure (a) is an image of the transparent electrode membrane device. The scale at left is indicated in cm. The membrane is circular, 15 mm diameter, and is positioned beneath the transparent electrode. Voltage to the transparent electrode is accomplished by the blue wire shown in the figure. Right figure (b) illustrates the optical measurement and test experiment. The device is illuminated by a collimated laser beam and imaged by a Shack-Hartmann wavefront sensor.

The device was illuminated by a collimated, coherent source at near normal incidence; reflected light was passed to a Shack-Hartmann wavefront sensor for measurement and control, as illustrated in Figure 1b. The device operated in closed loop with the wavefront sensor and was used to generate pre-defined wavefront deformations as well as correct aberrations that were introduced into the input beam.

2. Device fabrication

Membranes were 15mm diameter circles and had 1 μm thickness. Membranes were fabricated from essentially un-doped, single crystal, silicon-on-insulator (SOI) wafers with extremely low (tensile) intrinsic stress. Previous measurements of the stress of similar membranes, based upon resonant frequency analysis, indicated the stress to be between 3-7 MPa. Low stress is a desirable feature for these devices because it enables highly flexible membranes that are easily deformed. Other common membrane materials include silicon nitride (typically 50-100 MPa stress), and polycrystalline silicon (typically 50 MPa stress).

Membrane wafers were processed starting from the back side of each wafer, and fabrication consisted of contact lithography and deep silicon etching. Wafers were diced with a combination of manual cleaving and processing with a scribe and break tool. The buried oxide was subsequently removed at chip level by rinsing with buffered oxide etch (7:1 HF solution). This procedure yielded defect free, circular membranes. The front surface of the wafer was not exposed to the etchant during this process, and no pin hole defects formed in the membranes. Completed membranes were flip chip bonded to electrode arrays.

The electrode arrays, which were fabricated separately, contained 1024 electrodes tiling a 10 mm diameter circular area. Individual electrodes were square, 275 μm wide, and adjacent electrodes were spaced 5 μm apart. Polyimide posts that were patterned on the electrode arrays formed the spacer between membrane and electrode chips. Spacer height was 19 μm for the device whose data are presented here.

A 450 Å thick aluminum film was evaporated on the front membrane surface after flip chip bonding, for broadband visible light reflectivity, while maintaining a flat (tensile) membrane. This procedure allowed the membrane to retain its important low tensile stress characteristic even after metal coating.

To enable actuation of the membrane in both directions (push and pull), a transparent electrode was placed some distance above the membrane. This approach was first demonstrated in a macro-machined device.[8] The transparent electrodes consisted of 300 μm thickness Borofloat ® glass that was ITO coated for electrical conductivity and visible light transmission. Data presented below were taken from a device with membrane-transparent electrode distance of 56 μm. Holes in the electrode, visible in Figure 1a, were intended to allow air passage over the membrane and thereby mitigate squeeze film damping; they were outside the active pupil of the device. Alignment of the transparent electrode was done manually under a microscope. Electrical connectivity was achieved by evaporating gold through the vent hole sidewall and connecting a narrow gauge wire to the front surface of the transparent electrode and sidewall using conductive epoxy.

After fabrication, devices were mounted in pin grid array packages, and wire bonded to allow electrical connection to the electrodes of the array. In this prototype, approximately 60% of wire bonds were completed. The un-bonded electrodes occurred predominantly in one quadrant of the device; and the resulting asymmetrical control of the membrane as well as charging of un-bonded electrodes undoubtedly adversely affected the device performance.

3. Measurement & Test Experiment

The optical layout illustrated in Figure 1b was used to test membrane mirror devices in open and closed loop experiments. The incident, collimated beam could have a source of wavefront aberration optionally introduced into the system. Light reflected from the membrane was passed to the Shack-Hartmann wavefront sensor[*], which sampled the 15 mm diameter pupil with a 30x30 lenslet array.

Measurements of the un-powered membrane typically had 10-20 nm RMS wavefront aberration. This figure indicated the precision of the wavefront measurement not the intrinsic membrane flatness, because the Shack-Hartmann sensor was only capable of a relative

---

[*] Wavescope model from Adaptive Optics Associates

measurement, and in this optical layout the reference and measurement wavefronts were identical.

Wavefront gradient information from the wavefront sensor was used to determine voltages of the membrane mirror device using standard methods of wavefront reconstruction and control.[9] A poke matrix was found by applying voltages to each of the actuators in turn and measuring the resulting wavefront response; this matrix was inverted in a least squares sense, using singular value decomposition, to form the wavefront reconstructor, R.

The control loop of the system was a simple integrator, which computed the new actuator drive signals, x_{n+1} at each iteration, n, from the previous drive signals, x_n, by addition of a correction term δx_n. This correction term was found from the difference between the desired wavefront and the current measured wavefront, δb, multiplied by the reconstructor, R, and an adjustable gain parameter, g, according to

$$\delta x_n = gR \cdot \delta b \qquad (1)$$

This procedure was found to converge toward the desired wavefront under suitable conditions. After insertion of a source of wavefront aberrations into the incident beam, and setting the control loop to converge to a flat wavefront, the system was programmed to remove the distortions from the beam. Without the aberrations to the input beam, the device could be programmed to converge to pre-defined shapes such as Zernike polynomials.

The device was operated according to the following sequence of steps: First, the wavefront sensor was calibrated with no voltages applied to the device. Then the device "poke matrix" was established by applying voltage to each actuator (or binned actuator) in turn and measuring the wavefront response; pseudo-inversion of this matrix using singular value decomposition yielded the reconstructor. Then, prior to closed loop operation, voltage was applied to the transparent electrode to bias the membrane. The control loop compensated for this bias voltage while allowing deformation of the membrane away toward the transparent electrode array (ie above the "flat" position) during closed loop operation.

Operating voltages for transparent electrode and electrode array were in the 20-80 V range, typically. Too high a voltage being applied to electrodes of the array resulted in snap down of the membrane; this condition occurred on a number of occasions over the course of testing, from which the devices recovered without obvious defect.

4. Results

4.1 Zernike polynomial wavefront generation

Selected Zernike modes were generated in software; then the closed loop algorithm was used to command the device to each desired wavefront. The wavefronts illustrated below were stable, ie after stopping the close loop procedure, the optical wavefront remained stationary, and the device did not tend toward snap down. The device was able to approximate the illustrated Zernike modes, with nearly 10 μm peak-to-valley optical wavefront deformation.

Data below were taken with the device operating in 4x4 electrode binning mode, which corresponded to approximately 70 control channels. Figure 2 illustrates Zernike tilt, Figure 2(a) and 2(b), and spherical aberration, Figure 2(c) and 2(d), wavefronts including target wavefronts and experimental realizations. The entire 15 mm diameter wavefronts were illustrated in the figures; however, comparison statistics were computed within the central 10 mm diameters, corresponding to the active pupil of the device. The target tilt wavefront, Figure 2(a), had peak-to-valley and RMS wavefront deformations of 3.53 μm and 0.84 μm respectively; the corresponding experimental realization, Figure 2(b), had peak-to-valley and RMS wavefront deformations of 3.68 μm and 1.10 μm respectively. The target spherical aberration wavefront, Figure 2(c), had peak-to-valley and RMS wavefront deformations of

4.50 μm and 1.36 μm respectively; the corresponding experimental realization, Figure 2(d), had peak-to-valley and RMS wavefront deformations of 4.67 μm and 1.18 μm respectively.

Noise pixels that are apparent in the wavefront reconstructions arose from imperfections in the metallization of this particular device. The asymmetrical depression of the spherical aberration wavefront, Figure 2(d), reflects difficulty encountered in control of the device, undoubtedly resulting from charging of non-instrumented electrodes, as discussed above. These limitations are attributed to the particular device presented here, and they are not characteristic of these devices in general. Other fabricated devices that have been tested in the laboratory did not exhibit either of these defects.

Figure 3 illustrates the capability of the device to generate higher order Zernike modes with large amplitude. A trefoil pattern, Zernike No. 18[*], is illustrated in Figures 3 and 4. Within the central 10 mm diameter, the target wavefront, Figure 3(a), had peak-to-valley and RMS wavefront deformations of 6.25 μm and 1.52 μm respectively; the corresponding experimental realization, Figure 3(b), had peak-to-valley and RMS wavefront deformations of 7.29 μm and 2.03 μm respectively. A Zernike decomposition of the data from Figure 3(a) and 3(b), is shown in Figure 3(c). The solid line in Figure 3(c) illustrates coefficients of an a posteriori Zernike decomposition of the target wavefront; circles indicate a similar decomposition of the experimental realization. The Zernike decomposition demonstrates that the desired Zernike mode is represented with the greatest amplitude in the experimental wavefront. In this decomposition, a lower order trefoil, Zernike No. 9, is the next largest coefficient. The presence of other low order components reflects the lack of complete control of the wavefront and is attributed to the aforementioned charging of non-instrumented electrodes.

Wavefront deformations approaching 10 μm for the trefoil pattern were obtained with this device. A surface plot of one such wavefront is illustrated in Figure 4. Within the central 10 mm diameter, these data had peak-to-valley and RMS deformations of 9.31 μm and 2.90 μm (and 9.98μm and 2.39 μm respectively over the entire 15 mm wavefront).
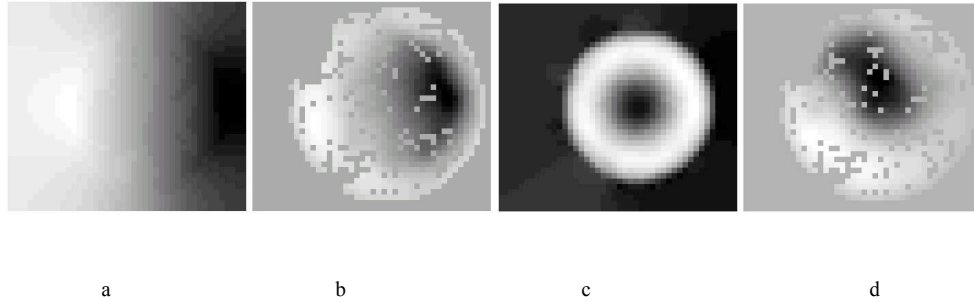

a   b   c   d

Figure 2 a, b, c, d. Left figure (a) illustrates target wavefront, tilt. Middle left figure (b) illustrates a realization of tilt produced by the deformable mirror. Middle right figure (c) illustrates target wavefront, spherical aberration. Right figure (d) illustrates a realization of spherical aberration produced by the deformable mirror.

---

[*] The Zernike polynomials referenced in this paper follow the convention adopted in reference 10 (Zygo Zernikes); according to this convention $Z_{18} \equiv \left(5r^2 - 4\right)r^3 \cos\left(3\phi\right)$
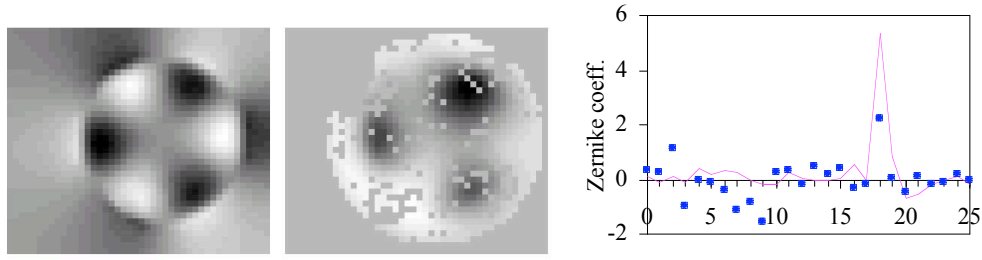
Figure 3 a,b,c. Left figure (a) illustrates target wavefront, Zygo Zernike 18. Middle figure (b) illustrates a realization of Zenike 18 produced by the deformable mirror. Right figure (c) illustrates Zernike decomposition, coefficient value vs. index number, of the target (solid line) and experiment realization (filled circles).
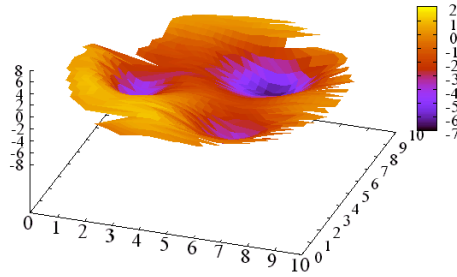

Figure 4. Surface plot illustrating nearly 10 μm peak-to-valley wavefront deformation for a trefoil pattern (Zygo Zernike 18) generated by the deformable mirror. X,Y axes in mm, Z axis in μm.

4.2 Total deformation and voltage vs. deflection characteristics

The membrane device demonstrated control of the optical wavefront over a 50 μm range, corresponding to 90 wavelengths, under stable operation. Maximum deformations toward the transparent electrode were estimated at 30 μm optical using the voltage-deflection model discussed below; however, reliable measurements were limited to less than 20 μm by spot confusion in the wavefront sensor.   Deformations of 20 μm optical toward the electrode array were obtained. These data were used to generate the mechanical deflection vs. voltage characteristics of the membrane device, in Figure 5.

The maximum deformation toward the electrode array corresponds to approximately 10 μm mechanical deformation, which is greater than the well known 1/3 gap snap down limit[*] for this device. Calculations of the stability of the membrane device under these conditions corroborate that membrane should be stable to this limit of deformation.[11]

---

[*] Mechanical devices under electrostatic actuation become unstable when the deformation is 1/3 the total gap distance. This result is exact only for rigid plates, not membranes.

The data of Figure 5 illustrate the deformation above and below the flat membrane position in response to voltages applied to the transparent electrode and the electrode array. These data were obtained by applying a voltage to the transparent electrode, Figure 5(a), or a uniform voltage to all electrodes of the array, Figure 5(b), (other voltages were fixed at ground) and measuring the resulting optical wavefront deformation. Mechanical deflections were obtained by dividing the optical wavefront data by two, to compensate for double pass (reflection) of the optical wavefront. The membrane deflection data have random measurement errors comparable to the symbol size in Figure 5; above 10 μm (corresponding to 20 μm optical), the data have a systematic error resulting in under-measurement of the wavefront deformation due to spot confusion in the wavefront sensor. The data show an expected quadratic dependence in the 0-10 μm range.
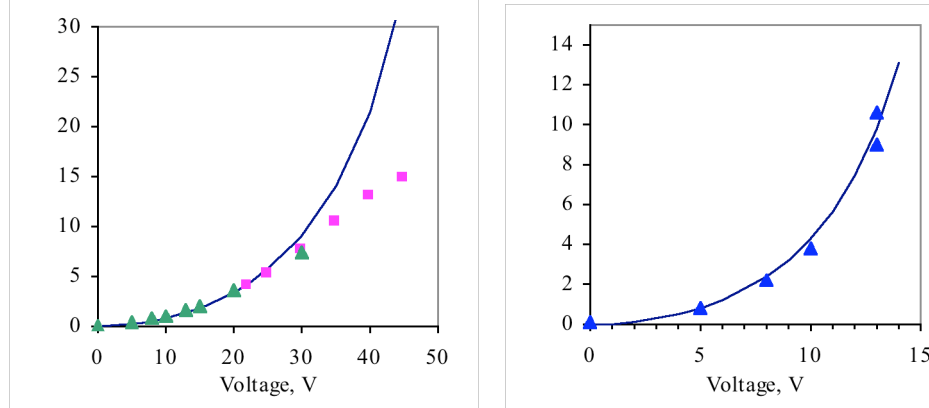

Figure 5 a,b. Entire membrane deflection (mechanical) vs. voltage data. Left figure (a) illustrates deflection (in microns) toward transparent electrode as a function of transparent electrode voltage. Data for deflections greater than 10 microns are under-estimates of the actual deflection due to limitations of the wavefront sensor. Model (solid curve) has 3 MPa membrane stress. Right figure (b) illustrates deflection (in microns) toward electrode array as a function of electrode array voltage. Model (solid curve) has 3 MPa membrane stress.

The data in Figure 5 are compared to an analytical model of the membrane deformation that has been successful in describing the general characteristics of previous membrane devices. This model consists of a solution of the Poisson equation of equilibrium for the membrane, with the electrostatic pressure approximated to 1'st order in the membrane deformation. Components of the model include membrane-electrode distance (19 μm), membrane-transparent electrode distance (56 μm), and other geometrical parameters. The membrane stress is a free parameter of the model; the curves indicated in Figure 5 correspond to a stress of 3 MPa. Previous direct measurements of the stresses of similar membranes placed this value at 3-7 MPa.

4.3 Correction of wavefront aberrations

To test the ability of the device to correct wavefront aberrations, an aberrating phase screen was improvised. This aberrator consisted of a microscope slide that had been treated with several thin coats of commonly available hair spray;[*] it was inserted into the incident laser beam before the deformable mirror as indicated in Figure 1b. The aberrated wavefront had 7367 nm peak-to-valley and 1886 nm RMS optical deformation, see Table 1 and Figure 6. In comparison, the calibration wavefront, measured without the aberrator but otherwise identical optical configuration had 66 nm peak-to-valley and 16 nm RMS optical deformation.

---

[*] Revlon brand Osis hairspray

The deformable mirror was used to correct the aberrations in the following manner: First a voltage was applied to the transparent electrode (20 V in this experiment). The resulting wavefront had approximately 10 μm peak-to-valley deformation. Then the closed loop algorithm was used to flatten the wavefront by applying voltages to the electrode array. 4x4 electrode binning was used.

The deformable mirror was able to partially correct the aberrations that were introduced into the beam. The corrected wavefront had an RMS deformation of 475 nm (4x improvement), see Table 1 and Figure 7.

The mirror is able to best correct large, low order aberrations, particularly with amplitude greater than 10 μm. The mirror does not perform well on low amplitude, high spatial frequency aberrations. Incomplete instrumentation of the electrodes of the array undoubtedly contributed two deleterious effects: charging and lack of voltage control of the non-instrumented electrodes.

Wavefront description	PV	RMS
calibration	66	16
aberrated	7367	1886
corrected	2505	475

Table 1. Wavefront statistics, in nanometers, for the aberration correction experiment. These statistics were computed for the central 10 mm diameter region of the entire 15 mm diameter wavefront.
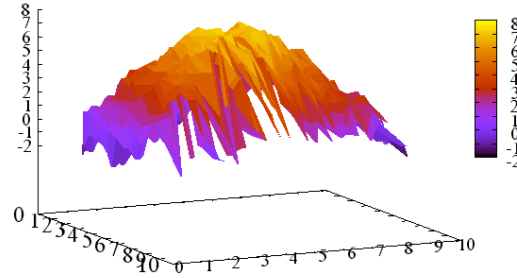

Figure 6. Aberrated optical wavefront. Only the central 10 mm diameter region of the entire optical pupil is illustrated here. X,Y axes in mm, Z axis in microns.
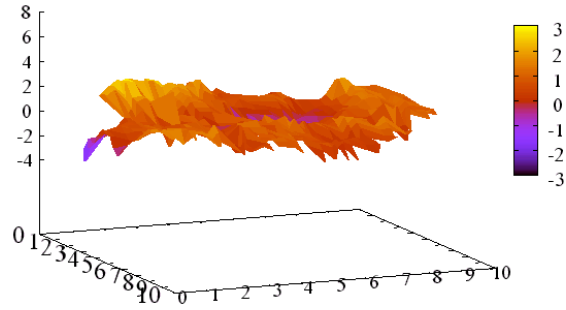
Figure 7. Corrected optical wavefront. Only the central 10 mm diameter region of the entire optical pupil is illustrated here. X,Y axes in mm, Z axis in microns.

5. Conclusion

The membrane device presented here consisted of a low stress membrane that was controlled by a 1024 electrode array and a transparent counter-electrode. The use of a transparent electrode enabled generation of membrane deformations above the un-deformed, flat position.

This membrane device demonstrated large (+/- 20 μm peak-to-valley optical) low order deformation, and nearly 10 μm peak-to-valley optical deformation for high order deformations. For high spatial order deformations, this figure is an order of magnitude improvement over previous micro-fabricated membrane mirrors.[4] Partial correction of wavefront aberrations was also demonstrated.

Together these results demonstrate that membrane devices are capable of large amplitude deformations and that they are not limited by bending stress to very small amplitude deformations, as has been previously supposed.

We attribute the limitations of the device to the lack of complete instrumentation of electrodes of the array; un-instrumented electrodes could not be actively controlled and experienced charging, which further impeded the effectiveness of wavefront control. There is promise that future devices, when fully instrumented, would exhibit greater ability to correct and to generate high spatial frequency deformations with significant amplitude, and to correct corresponding aberrations to the diffraction limit. These membrane devices would have significant utility for ophthalmic and astronomical adaptive optics applications.